Rapid infrared imaging of rhombohedral graphene

Zuo Feng,[1,2,§] Wenxuan Wang,[2,§] Yilong You,[1,2,§] Yifei Chen,[3] Kenji Watanabe,[4] Takashi Taniguchi,[5] Chang Liu,[1,2,†] Kaihui Liu,[1,2,‡] and Xiaobo Lu[2,6,*]

[1] *State Key Laboratory for Mesoscopic Physics, Frontiers Science Centre for Nano-optoelectronics, School of Physics, Peking University, Beijing 100871, China*

[2] *International Center for Quantum Materials, School of Physics, Peking University, Beijing 100871, China*

[3] *International School of Beijing, Beijing 101318, China*

[4] *Research Center for Electronic and Optical Materials, National Institute of Material Sciences, 1–1 Namiki, Tsukuba 305-0044, Japan*

[5] *Research Center for Materials Nanoarchitectonics, National Institute of Material Sciences, 1–1 Namiki, Tsukuba 305-0044, Japan*

[6] *Collaborative Innovation Center of Quantum Matter, Beijing 100871, China*

(Received 17 August 2024; revised 30 January 2025; accepted 4 February 2025; published 6 March 2025)

The extrinsic stacking sequence based on intrinsic crystal symmetry in multilayer two-dimensional materials plays a significant role in determining their electronic and optical properties. Compared with Bernal-stacked (ABA) multilayer graphene, rhombohedral (ABC) multilayer graphene hosts stronger electron-electron interaction due to its unique dispersion at low-energy excitations and has been utilized as a unique platform to explore strongly correlated physics. However, discerning the stacking sequence via scanning mapping methods has always been a fairly time-consuming process. Here, we report a rapid recognition method for ABC-stacked graphene with high accuracy by infrared imaging based on the distinct optical responses in the infrared range. The optical contrast of the image between ABC- and ABA-stacked graphene is strikingly clear, and the discernibility is comparable to traditional optical Raman microscopy but with higher consistency and throughput. We demonstrate that the infrared imaging technique can be integrated with dry transfer techniques commonly used in the literature. This rapid and convenient infrared imaging technique will significantly improve the sorting efficiency for differently stacked multilayer graphene, thereby accelerating the exploration of the novel emergent correlated phenomena in ABC-stacked graphene.

DOI: 10.1103/PhysRevApplied.23.034012

I. INTRODUCTION

Rhombohedral (ABC) stacked multilayer graphene has been a highly tunable platform for exploring strongly correlated and topological phenomena. At low-energy excitation, the dispersion of ABC-stacked multilayer graphene follows the relation of $E = Ap^N$ for single-particle level, where E is the kinetic energy, A is a constant, p is the momentum, and N is the number of layers. The unique band dispersion leads to a strong correlation between electrons dominating over their kinetic energy at low Fermi energy, particularly for the layer number $N \geq 3$ [1–8]. In recent years, a plethora of novel correlated phenomena have come to light in ABC-stacked graphene systems, including Mott insulators [5], layer-polarized antiferromagnetic insulators [9–11], superconductivity [12,13], Stoner ferromagnetism [14], orbital multiferroicity [15], integer Chern insulators [16–18], and fractional Chern insulators [19] based on a small number of devices reported by several laboratories. So far, the fabrication of standard ABC graphene devices compatible with transport measurement is still challenging due to two reasons: (i) the energetically metastable ABC-stacked sequence will easily relax into Bernal-stacked (ABA) sequence with lower energy during the fabrication processes; (ii) identifying ABC-stacked region of graphene flakes is time-consuming and involves scanning techniques, such as scanning near-field optical microscopy [20–22], scanning Raman spectroscopy [23–25], scanning Kelvin probe microscopy [26], second harmonic generation [27,28], and angle-resolved photoemission spectroscopy [29]. Developing a rapid detection method for discerning the graphene stacking sequence, both before and after the assembly process of

*Contact author: xiaobolu@pku.edu.cn
†Contact author: liu.chang@pku.edu.cn
‡Contact author: khliu@pku.edu.cn
§Z.F., W.W., and Y.L. contributed equally to this work.

the heterostructures, would significantly facilitate device fabrication.

In this study, we report a real-time imaging method for rapidly distinguishing the stacking sequence of multilayer graphene in the infrared range. The infrared imaging technique provides high-quality images of differently stacked domains (ABC or ABA stacking) with a resolution better than 1 μm, consistent with results obtained from Raman spectroscopy mapping. In multilayer graphene, more complex stacking orders can also be distinguished, such as ABAB, ABCA, and ABCB configurations in tetralayer graphene. Moreover, the stacking sequence can also be distinguished when graphene flakes are encapsulated with hBN flakes, allowing for convenient monitoring of stacking sequence changes during the assembly process.

II. METHODS

In ABC-stacked graphene, the second layer atoms sit in the center of the hexagonal lattice of the first layer atoms, and the third layer atoms continue to shift in the same direction. In contrast, in ABA-stacked graphene, the third layer aligns directly above the first layer [Figs. 1(a) and 1(b)]. The different stacking sequences result in radically different band structures for multilayer graphene [30,31]. For tetralayer graphene, ABA-stacked graphene has two hyperbolic bands near the K-point and two split-off bands, while ABC graphene has one hyperbolic band and three split-off bands [Figs. 1(c) and 1(d)]. Details of the tight-binding calculation are shown in Appendix A. The optical conductivity of a material arises from two distinct types of absorption mechanisms: intraband absorption and interband absorption. An interband transition describes the process in which an electron absorbs a photon and jumps from the valence band to the conduction band directly. An intraband absorption requires the scattering with phonons to satisfy the momentum conservations. In graphene, optical conductivity is primarily attributed to the intraband transitions in the far-infrared region. In contrast, for visible and near-infrared wavelengths, optical conductivity is predominantly determined by the interband transitions [32–36]. In Figs. 1(e) and 1(f), we plot the interband transition distribution for photons with an energy of 0.78 eV (corresponding to a wavelength of 1600 nm) for ABC-tetralayer graphene with two different stacking sequences. For ABC-stacked graphene, the transition from the V1

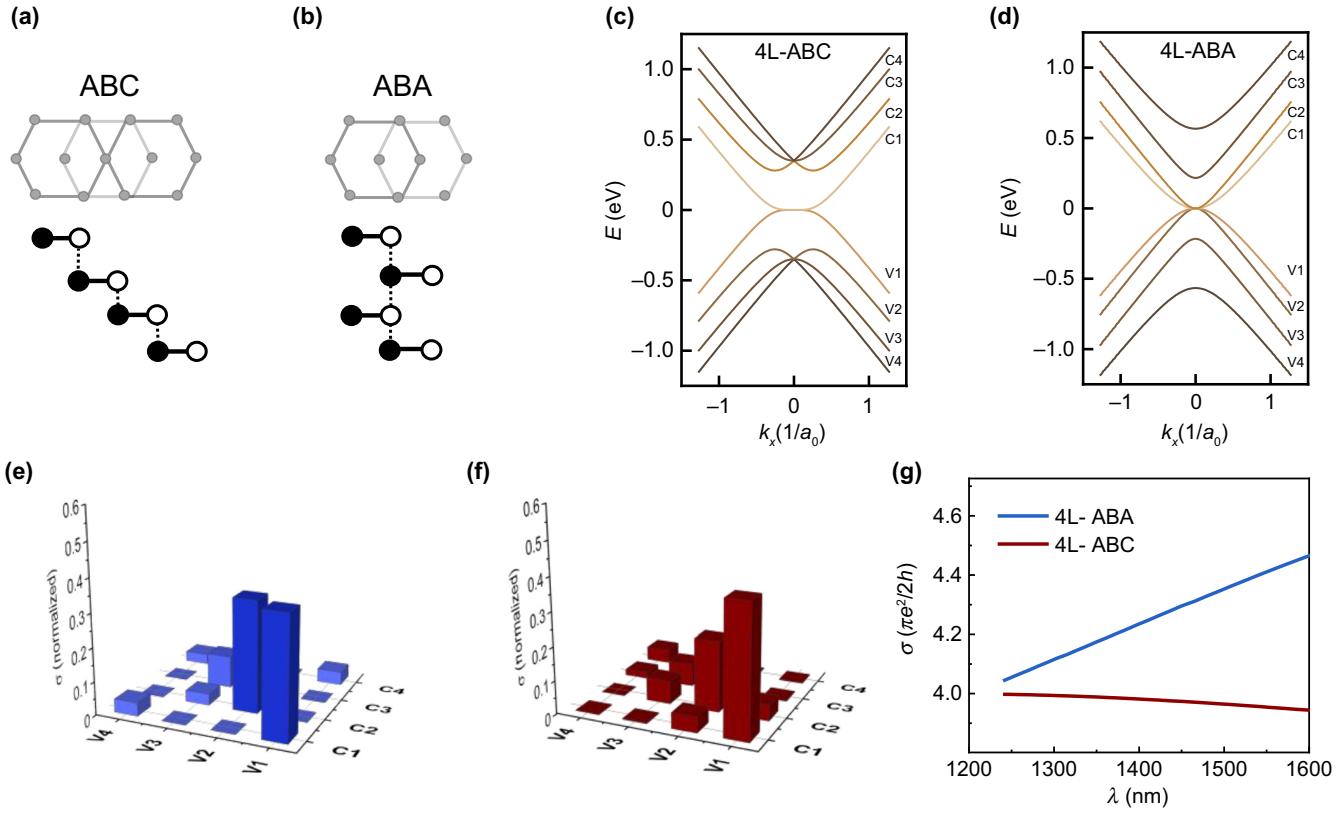

FIG. 1. Different optical reflectance in the infrared range of tetralayer ABC and ABA graphene. (a) Atomic structures of rhombohedral ABC-stacked graphene. (b) Atomic structures of Bernal ABA-stacked graphene. (c) Band structure of ABC-tetralayer graphene. (d) Band structure of ABA-tetralayer graphene. (e) Contributions of different band transitions to optical conductivity of ABC-tetralayer graphene at 1600 nm. (f) Contributions of different band transitions to optical conductivity of ABA-tetralayer graphene at 1600 nm. (g) Calculation results of the optical conductivity of ABA- and ABC-tetralayer graphene.

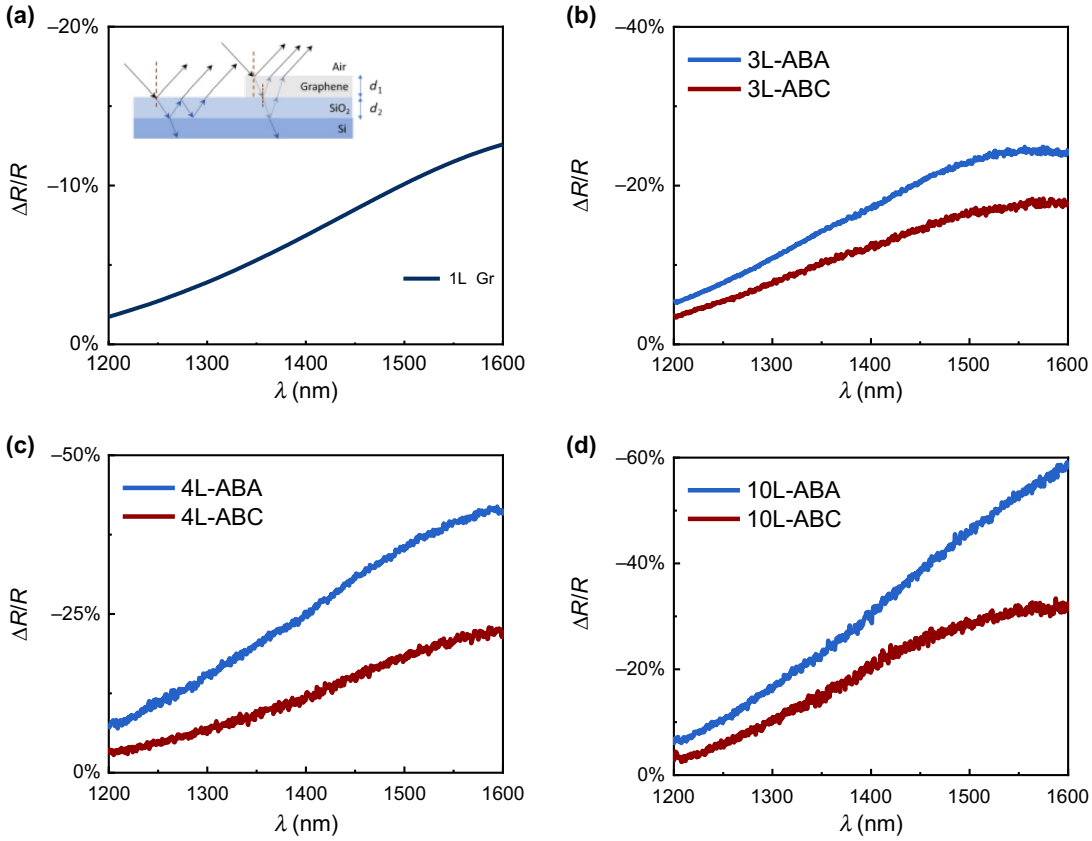

FIG. 2. Differential reflectance spectroscopy of ABA and ABC graphene. (a) Calculated contrast of monolayer graphene considering multireflection. Inset: Schematic of multireflection model. Differential reflectance spectroscopy of (b) ABA- and ABC-trilayer graphene, (c) tetralayer graphene, and (d) decalayer graphene.

band to the C1 band accounts for ∼40% of the optical conductivity contribution. The transition from the V2 band to the C2 band accounts for ∼25% of the optical conductivity contribution. For ABA-stacked graphene, the transition from the V1 band to the C1 band and from the V2 band to the C2 band both contribute approximately 40% of the optical conductivity. Details of the tight-binding calculation are shown in Appendix B. Considering all the optical transitions, ABC-stacked tetralayer graphene exhibits lower optical conductivity compared with ABA-stacked graphene in the infrared range [Fig. 1(g)]. The optical conductivity of ABC-stacked graphene decreases with increasing wavelength, while the optical conductivity of ABA-stacked graphene increases. Specifically, in the range of 1200 to 1600 nm, the conductivity of ABA-stacked graphene is consistently higher than that of ABC-stacked graphene.

III. RESULTS

We have further experimentally investigated the infrared properties of ABA- and ABC-stacked graphene (including trilayer, tetralayer, and decalayer graphene) with differential reflectance spectroscopy covering wavelengths from 1200 to 1600 nm. In our experiment, the multilayer graphene was exfoliated onto a highly doped silicon substrate with a 285-nm oxide layer, which is widely used in the literature. The stacking sequence was initially confirmed with the Raman spectrum. The differential reflectance $\Delta R/R$ is defined as $\Delta R/R = (R_{gr}–R_{sub})/R_{sub}$, where R_{gr} is the reflectance of graphene on the substrate and R_{sub} is the reflectance of bare substrate. Figure 2(a) shows the calculated differential reflectance $\Delta R/R$ considering the multireflection process for a monolayer graphene. We use a four-layer model composed of air (n_0), graphene (n_{gr}), silicon oxide (n_2), and silicon substrate (n_3). More details are shown in Appendix C. Theoretically, $R_{gr} = |(r_1 + r_2 e^{-2i\beta 1} + r_3 e^{-2i(\beta 1+\beta 2)} + r_1 r_2 r_3 e^{-2i\beta 2})/(1 + r_1 r_2 e^{-2i\beta 1} + r_1 r_3 e^{-2i(\beta 1+\beta 2)} + r_2 r_3 e^{-2i\beta 2})|^2$, where $r_1 = (n_0 - n_{gr})/(n_0 + n_{gr})$, $r_2 = (n_{gr} - n_2)/(n_{gr} + n_2)$, and $r_3 = (n_2 - n_3)/(n_2 + n_3)$ are the reflection coefficients between the interface, respectively. Moreover, $\beta_1 = 2\pi n_{gr} d_1/\lambda$ and $\beta_2 = 2\pi n_2 d_2/\lambda$ are the phase changes due to the different optical paths. The

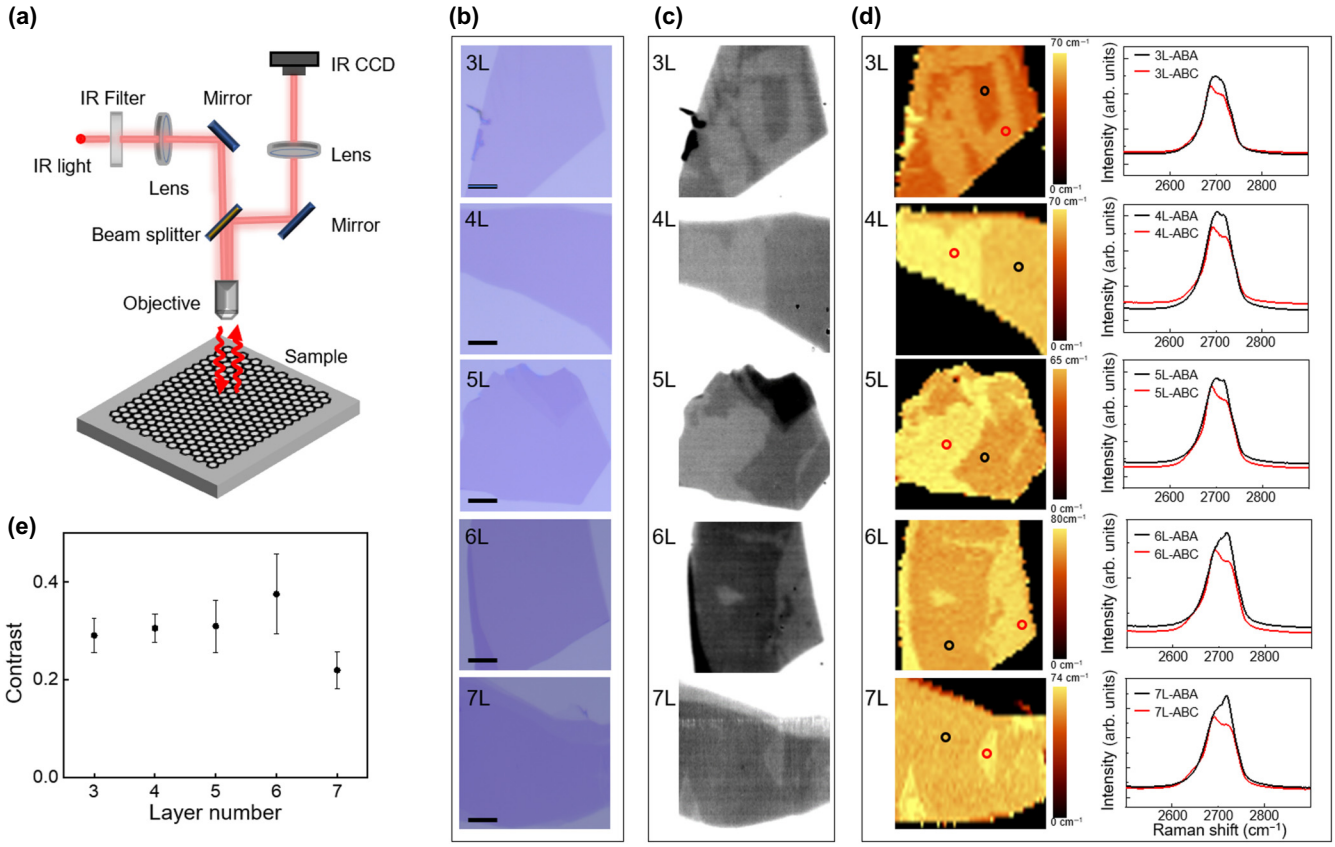

FIG. 3. Rapid infrared imaging system. (a) Schematic of infrared imaging system. (b) Optical image of graphene from trilayer to heptalayer. The scale bar is 6 μm. (c) Infrared image of the graphene flakes, as shown in (b). (d) Raman FWHM 2D mode mappings and Raman spectra of the same graphene flakes, as shown in (b),(c). Raman spectra for ABA-stacked (black) and ABC-stacked (red) graphene were extracted from Raman mapping with the positions indicated with little red circles. (e) Contrast difference in the infrared images between ABA and ABC graphene for different layers.

refractive index of graphene (n_{gr}) sensitively depends on the optical conductivity via the relation $\sigma = i\omega(n_{gr}{}^2 - \varepsilon_0)$, where ω is the frequency of incident light and ε_0 is the dielectric constant of vacuum. For multilayer graphene, different values of optical conductivity σ originate from different stacking sequences [Fig. 1(g)] can lead to distinct different values of $\Delta R/R$, as shown in Figs. 2(b)–2(d).

Based on the distinct differential reflectance results, we have further designed a real-time infrared imaging system to distinguish different stacking sequences of multilayer graphene. As shown in Fig. 3(a), the infrared light with effective wavelength $\lambda > 900$ nm achieved by a long-wave-pass filter is used for illumination. The reflected signal is collected through an objective with a magnification value of 100 and a numerical aperture value of 0.85. The signal is further recorded with an InGaAs CCD with a detection range from 900 to 1700 nm.

Representative graphene samples, ranging from trilayer to heptalayer graphene, were characterized with the infrared imaging system. Traditional optical images, shown in Fig. 3(b), reveal only uniform optical contrast. In contrast, the infrared imaging system provides sharp differentiation between ABC- and ABA-stacked graphene due to their distinct optical reflectance in the infrared range [Fig. 3(c)]. As illustrated in Fig. 3(c), the brighter regions correspond with ABC-stacked areas, while the darker regions correspond to ABA-stacked areas. The stacking order was confirmed by the Raman spectra [23]. ABC-stacked graphene shows a more asymmetric feature with a pronounced shoulder compared with ABA-stacked graphene around 2680 cm^{-1}. Full width at half maximum (FWHM) mapping of the 2D Raman mode, as shown in Fig. 3(d), was also used to independently verify regions with different stacking sequences. Notably, the infrared imaging results are highly consistent with Raman mapping. To demonstrate the universality of this imaging technique, different graphene samples with layer numbers ranging from trilayer to heptalayer were imaged. Contrast differences between different stacking sequences vary from 15% to 40%, enabling a straightforward identification [Fig. 3(e)].

Tetralayer graphene exhibits three types of stacking orders: ABAB, ABCA, and ABCB. The optical image [Fig. 4(a)] shows uniform contrast across the tetralayer

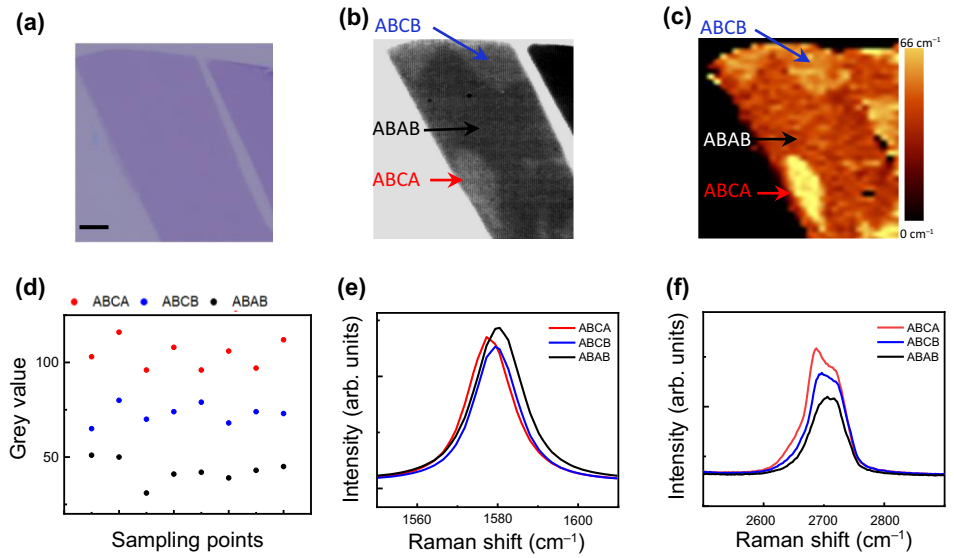

FIG. 4. Different stacking orders in tetralayer graphene. (a) Optical images of tetralayer graphene. The scale bar is 5 μm. (b) Infrared image of tetralayer graphene. (c) Raman mapping of the FWHM 2D mode of tetralayer graphene. (d) Gray value of tetralayer graphene with three stacking orders. (e) Raman spectra (G mode) of tetralayer graphene with three stacking orders. (f) Raman spectra (2D mode) of tetralayer graphene with three stacking orders.

graphene, with no visible differences. However, these stacking configurations display distinct contrasts under infrared imaging [Fig. 4(b)], allowing clear differentiation between the ABAB-, ABCA-, and ABCB-stacking orders. The ABAB stacking exhibits the lowest contrast and occupies the largest area, while the ABCA stacking displays the highest contrast. The ABCB stacking shows an intermediate contrast. We extracted the gray values for the three stacking orders from the infrared image [Fig. 4(d)], where a gray value of 1 corresponds to pure black and a gray value of 255 represents pure white. The average gray value for ABAB stacking is 42, the lowest among the three. The average gray value for ABCB stacking is 72, while ABCA stacking has an average gray value of 104. By comparing the grayscale contrasts of different regions in the infrared image, the various stacking configurations can be directly distinguished. The stacking orders were further confirmed through Raman spectroscopy, specifically by examining the G and 2D modes [24]. In ABCA-stacked graphene, the G mode shows a blue shift. The G mode positions of ABCB- and ABAB-stacked tetralayer graphene are similar, but the G mode peak of ABCB stacking is narrower than that of ABAB stacking. Notably, the 2D mode of these three stacking types in tetralayer graphene exhibits distinct characteristics: ABCA stacking shows the most asymmetric feature with a pronounced shoulder, ABAB stacking shows a symmetric 2D band with two peaks of nearly equal intensity, and ABCB stacking presents a profile between those of ABAB and ABCA stacking. Furthermore, our imaging technique is capable of distinguishing even more complex stacking orders in multilayer graphene (Appendix D). Four stacking orders can be resolved in heptalayer graphene. The average gray values in the 1, 2, 3, and 4 regions are 21, 41, 56, and 82, respectively. By comparing infrared images with Raman mapping, we observe that the brightest regions exhibit a more asymmetric 2D mode with an enhanced shoulder at around 2690 cm^{-1}, while the darkest regions show an enhanced shoulder at around 2720 cm^{-1}. However, as the heptalayer graphene contains more than four stacking configurations, we are unable to precisely identify the specific stacking types in the regions with intermediate contrast. We further demonstrate the infrared imaging system as a reliable and versatile technique for distinguishing graphene stacking sequences when encapsulated with hBN flakes (Appendix E). The ABC stacking region also shows a bright contrast. Utilizing the rapid infrared imaging technique, pure ABC stacking regions were accurately selected for further device fabrication. With the help of a rapid infrared imaging technique, several devices with thickness ranging from three to six layers were fabricated (Appendix F). All the devices exhibit the unique electrical properties of ABC-stacked graphene from previous studies [5,13,14,19].

IV. CONCLUSIONS

In summary, we have introduced a rapid imaging technique for identifying ABC-stacked graphene. The ABC-stacked regions exhibit a brighter contrast under infrared light compared with ABA-stacked regions on SiO_2/Si substrate. For thicker graphene layers, distinct stacking orders

exhibit unique contrasts. This technique also enables real-time identification of stacking sequences in graphene encapsulated by hBN throughout the fabrication process. However, we also note that there are still some inherent limitations of this rapid imaging technique. Firstly, as the number of layers increases, the stacking configurations beyond pure ABC and ABA become increasingly intricate, making it challenging to definitively identify each unique stacking sequence. Secondly, this imaging technique is limited by the diffraction limit, resulting in a lower imaging resolution than that of scanning probe techniques. We anticipate that this technique will significantly advance research on stacking order control and deepen the exploration of the strongly correlated physics emerging in ABC-stacked multilayer graphene.

ACKNOWLEDGMENTS

We acknowledge support from the National Key R&D Program of China (Grant No. 2022YFA1403500/02) and the National Natural Science Foundation of China (Grant No. 12141401, No. 52025023, No. 11888101, No. T2188101, No. 12304204).

X.L. and K.L. supervised the projects. Z.F. and W.W. fabricated the devices and performed the measurements. Y.Y., Y.C., and C.L. performed the theoretical modeling. K.W. and T.T. contributed materials. Z.F. and X.L. wrote the paper with input from all the authors.

APPENDIX A: CALCULATION OF BAND STRUCTURE

We use the tight-binding model to calculate the band structure of multilayer graphene. Here, we take the basis as $|A_1\rangle, |B_1\rangle; |A_2\rangle, |B_2\rangle; \ldots; |A_N\rangle, |B_N\rangle$. In order to capture the main features of our experiment data, we only consider the nearest intralayer hopping parameter γ_0 and interlayer hopping parameter γ_1. Then, the Hamiltonian around the K-point becomes

$$\mathcal{H} = \begin{pmatrix} H_0 & V & & & \\ V^\dagger & H_0 & V^\dagger & & \\ & V & H_0 & V & \\ & & \ddots & \ddots & \ddots \end{pmatrix}, \tag{A1}$$

with

$$H_0 = \begin{pmatrix} 0 & vp_- \\ vp_+ & 0 \end{pmatrix}, V = \begin{pmatrix} 0 & 0 \\ \gamma_1 & 0 \end{pmatrix}, \tag{A2}$$

where $p_\pm = p_x \pm ip_y$, with $\boldsymbol{p} = -i\hbar\nabla$, and the velocity of monolayer graphene is v. According to previous research, v relates to the band parameter through the equation $v = \sqrt{3}a\gamma_0/2\hbar$, H_0 describes the intralayer hopping, and V depicts the interlayer hopping. Here, we use $a = 0.246$ nm, $\gamma_0 = 3.16$ eV, and $\gamma_1 = 0.37$ eV.

Especially for 4-layer graphene, as is mentioned in the main text, the Hamiltonian for AB-stacked graphene is

$$\mathcal{H} = \begin{pmatrix} H_0 & V & & \\ V^\dagger & H_0 & V^\dagger & \\ & V & H_0 & V \\ & & V^\dagger & H_0 \end{pmatrix}, \tag{A3}$$

and the Hamiltonian for ABC-stacked graphene is

$$\mathcal{H} = \begin{pmatrix} H_0 & V & & \\ V^\dagger & H_0 & V & \\ & V^\dagger & H_0 & V \\ & & V^\dagger & H_0 \end{pmatrix}. \tag{A4}$$

APPENDIX B: CALCULATION OF OPTICAL CONDUCTIVITY

We employ the Kubo formula to calculate the optical conductivity, which is given as follows:

$$\sigma(\omega)_{i,j} = \frac{e^2\hbar}{iS} \sum_{b_1,b_2,\boldsymbol{k}} \frac{n_f\left(e^{\boldsymbol{k}}_{b_1}\right) - n_f\left(e^{\boldsymbol{k}}_{b_2}\right)}{e^{\boldsymbol{k}}_{b_1} - e^{\boldsymbol{k}}_{b_2}} \frac{e^{\boldsymbol{k}}_{b_1} |\mathbf{v}_i| e^{\boldsymbol{k}}_{b_2} e^{\boldsymbol{k}}_{b_2} |\mathbf{v}_j| e^{\boldsymbol{k}}_{b_1}}{\hbar\omega + e^{\boldsymbol{k}}_{b_1} - e^{\boldsymbol{k}}_{b_2} + i\eta}, \tag{B1}$$

where $e^{\boldsymbol{k}}_b$ are the eigenenergies of the Hamiltonian in band b at momentum point k and $|e^k_b\rangle$ are the corresponding eigenvectors. Here, n_f refers to the Fermi–Dirac distribution.

In our calculations, we only consider the x-direction optical conductivity $v_x = -(i/\hbar)[x, \mathcal{H}] = \partial\mathcal{H}/\partial p_x$. While obviously $\partial V/\partial p_x = 0$, which means v_x is written as

$$v_x = \begin{pmatrix} \partial H_0/\partial p_x & & & \\ & \partial H_0/\partial p_x & & \\ & & \partial H_0/\partial p_x & \\ & & & \partial H_0/\partial p_x \end{pmatrix}. \tag{B2}$$

Here, we use $\eta = 20$ meV and $T = 300$ K in our calculations.

APPENDIX C: CALCULATION OF MULTIREFECTION PROCESS

To explain the contrast change of graphene on SiO_2/Si substrate, we use Fresnel's equations. The multireflection model is composed of graphene, SiO_2, and silicon layers. The light is incident from air onto the three layers, and the reflected light intensity can be calculated using the following equations:

$$R_{\mathrm{gr}} = \left| \frac{r_1 + r_2 e^{-2i\beta_1} + r_3 e^{-2i(\beta_1+\beta_2)} + r_1 r_2 r_3 e^{-2i\beta_2}}{1 + r_1 r_2 e^{-2i\beta_1} + r_1 r_3 e^{-2i(\beta_1+\beta_2)} + r_2 r_3 e^{-2i\beta_2}} \right|^2, \tag{C1}$$

$$R_{\mathrm{sub}} = \left| \frac{(r_2 + r_3 e^{-2i\beta_2})}{1 + r_2 r_3 e^{-2i\beta_2}} \right|^2, \tag{C2}$$

$$\frac{\Delta R}{R} = \frac{R_{\mathrm{gr}} - R_{\mathrm{sub}}}{R_{\mathrm{sub}}},$$

where

$$r_2 = \frac{n_{gr} - n_3}{n_{gr} + n_3}, r_2 = \frac{n_{gr} - n_3}{n_{gr} + n_3}, r_3 = \frac{n_2 - n_3}{n_2 + n_3},$$

$$\beta_1 = 2\pi n_{gr} d_1/\lambda,\ \beta_2 = 2\pi n_2 d_2/\lambda.$$

This is possible because the refractive index can be described by the following equation:

$$\sigma = i\omega(n_{gr}^2 - \varepsilon_0),$$

where σ is the optical conductivity of graphene, ω is the frequency of the incident light, and ε_0 is the dielectric constant of vacuum.

The reflected light intensity, dependent on optical conductivity, can be described by the following equation:

$$R_{\mathrm{gr}}(\sigma) = \left| \frac{\left(n_0 - \sqrt{\frac{\sigma}{i\omega} + \varepsilon_0}\right)}{\left(n_0 + \sqrt{\frac{\sigma}{i\omega} + \varepsilon_0}\right)} + \frac{\left(\sqrt{\frac{\sigma}{i\omega} + \varepsilon_0} - n_2\right)}{\left(\sqrt{\frac{\sigma}{i\omega} + \varepsilon_0} + n_2\right)} e^{-2i\beta_1} + \frac{(n_2 - n_3)}{(n_2 + n_3)} e^{-2i(\beta_1+\beta_2)} + \frac{\left(n_0 - \sqrt{\frac{\sigma}{i\omega} + \varepsilon_0}\right)\left(\sqrt{\frac{\sigma}{i\omega} + \varepsilon_0} - n_2\right)}{\left(n_0 + \sqrt{\frac{\sigma}{i\omega} + \varepsilon_0}\right)\left(\sqrt{\frac{\sigma}{i\omega} + \epsilon} + n_2\right)} \frac{(n_2 - n_3)}{(n_2 + n_3)} e^{-2i\beta_2}}{1 + \frac{\left(n_0 - \sqrt{\frac{\sigma}{i\omega} + \varepsilon_0}\right)}{\left(n_0 + \sqrt{\frac{\sigma}{i\omega} + \varepsilon_0}\right)} \frac{\left(\sqrt{\frac{\sigma}{i\omega} + \varepsilon_0} - n_2\right)}{\left(\sqrt{\frac{\sigma}{i\omega} + \varepsilon_0} + n_2\right)} e^{-2i\beta_1} + \frac{\left(n_0 - \sqrt{\frac{\sigma}{i\omega} + \varepsilon_0}\right)(n_2 - n_3)}{\left(n_0 + \sqrt{\frac{\sigma}{i\omega} + \varepsilon_0}\right)(n_2 + n_3)} e^{-2i(\beta_1+\beta_2)} + \frac{\left(\sqrt{\frac{\sigma}{i\omega} + \varepsilon_0} - n_2\right)}{\left(\sqrt{\frac{\sigma}{i\omega} + \varepsilon_0} + n_2\right)} \frac{(n_2 - n_3)}{(n_2 + n_3)} e^{-2i\beta_2}} \right|^2 \tag{C3}$$

$$R_{\mathrm{sub}} = \left| \frac{\frac{\left(\sqrt{\frac{\sigma}{i\omega} + \varepsilon_0} - n_2\right)}{\left(\sqrt{\frac{\sigma}{i\omega} + \varepsilon_0} + n_2\right)} + \frac{(n_2 - n_3)}{(n_2 + n_3)} e^{-2i\beta_2}}{1 + \frac{\left(n_0 - \sqrt{\frac{\sigma}{i\omega} + \varepsilon_0}\right)}{\left(n_0 + \sqrt{\frac{\sigma}{i\omega} + \varepsilon_0}\right)} \frac{(n_2 - n_3)}{(n_2 + n_3)} e^{-2i\beta_2}} \right|^2. \tag{C4}$$

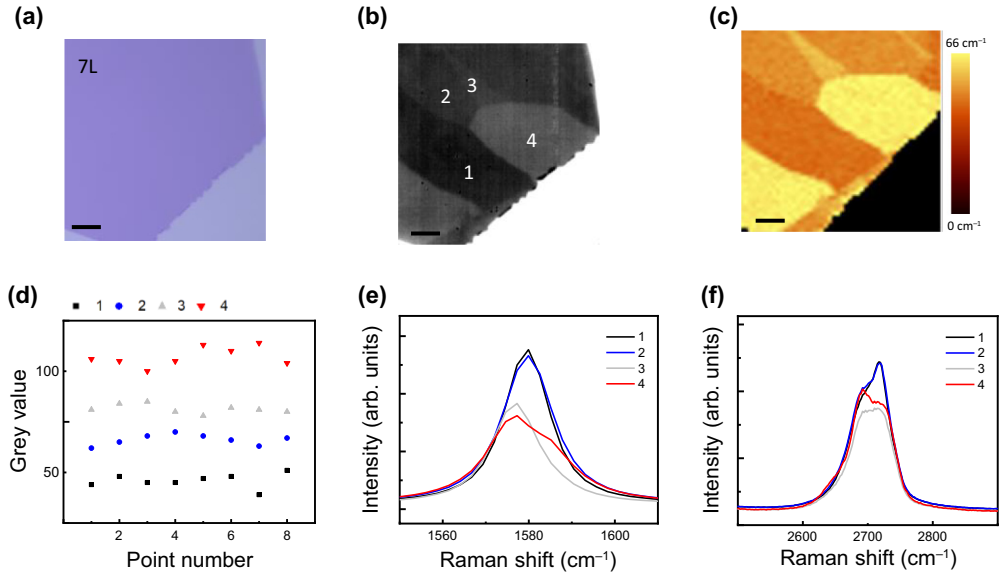

FIG. 5. Different stacking orders in heptalayer graphene. (a) Optical images of heptalayer graphene. The scale bar is 5 μm. (b) Infrared image of heptalayer graphene. (c) Raman mapping of the FWHM 2D mode of heptalayer graphene. (d) Gray value of heptalayer graphene with four stacking orders. (e) Raman spectra (G mode) of heptalayer graphene with four stacking orders. (f) Raman spectra (2D mode) of heptalayer graphene with four stacking orders.

APPENDIX D: DIFFERENT STACKING ORDERS IN HEPTALAYER GRAPHENE

Here, we demonstrate the contrast situations of different stackings of heptalayer graphene under infrared imaging. Four stacking orders can be resolved in heptalayer graphene. The average gray values in the 1, 2, 3, and 4 regions are 21, 41, 56, and 82, respectively. By comparing infrared image with Raman mapping, we observe that the brightest regions exhibit a more asymmetric 2D mode with an enhanced shoulder around 2690 cm^{-1} whereas the darkest regions show an enhanced shoulder around 2720 cm^{-1} (Fig. 5).

APPENDIX E: GRAPHENE STACKING SEQUENCES WHEN ENCAPSULATED WITH hBN FLAKES

Here, we demonstrate the infrared imaging system as a reliable and versatile technique for distinguishing graphene stacking sequences when encapsulated with hBN flakes. The ABC stacking region also shows a bright contrast (Fig. 6).

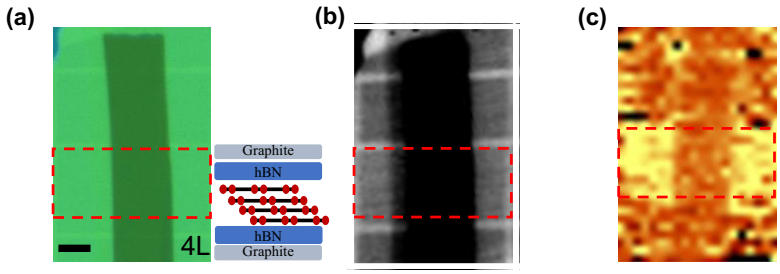

FIG. 6. Graphene stacking sequences when encapsulated with hBN flakes. (a) Optical image of tetralayer graphene encapsulated with hBN flakes and the schematic of the sample. The scale bar is 3 μm. (b) Infrared image of tetralayer graphene encapsulated with hBN flakes. (c) Raman mapping of tetralayer graphene encapsulated with hBN flakes.

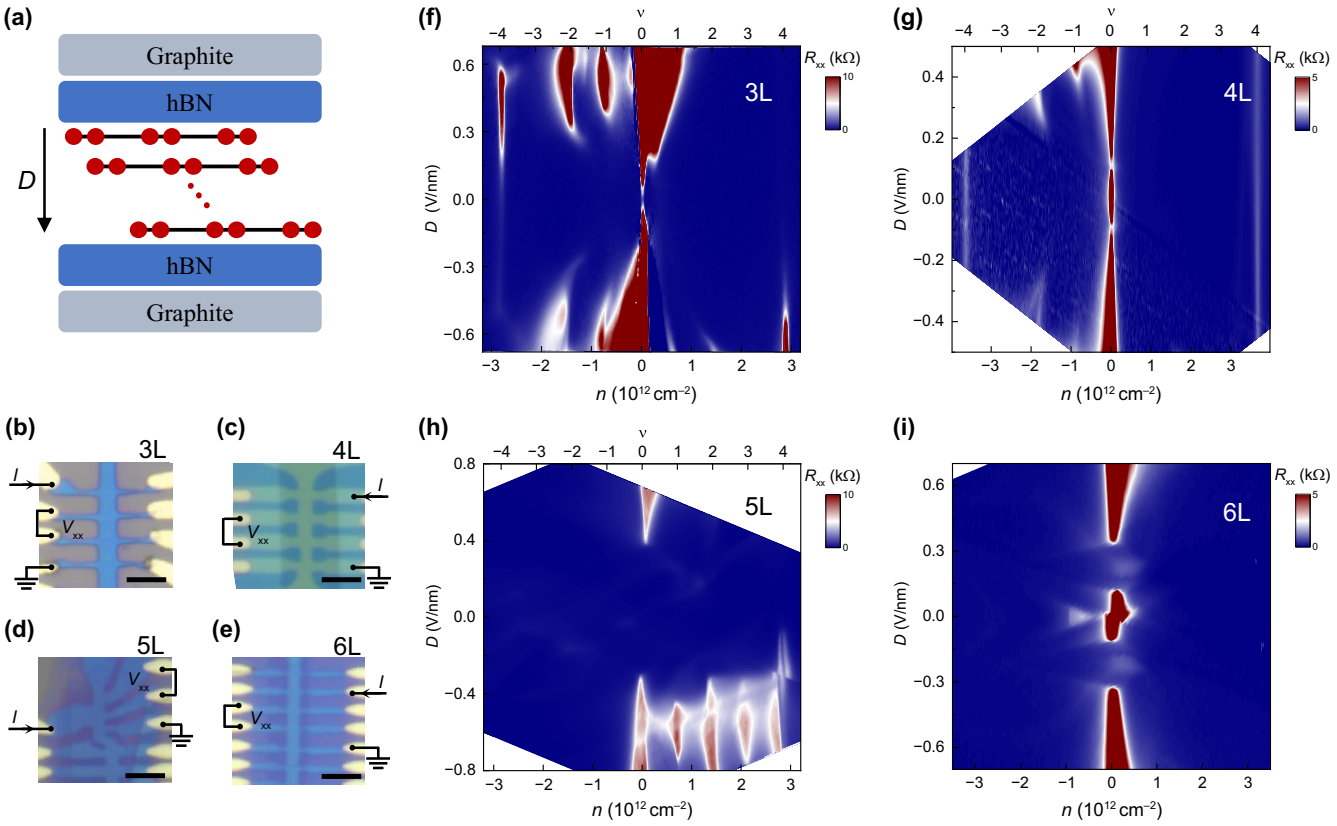

FIG. 7. Transport measurement of four different layered ABC-stacked graphene. (a) Schematic of the dual-gated device. Optical images of (b) trilayer graphene, (c) tetralayer graphene, (d) pentalayer graphene, and (e) hexalayer graphene. The scale bar is 5 μm. (f)–(h) Color plot of R_{xx} as a function of moiré filling ν and displacement field D for (f) trilayer graphene, (g) heptalayer graphene, and (h) pentalayer graphene. (i) Color plot of R_{xx} as a function of carrier density n and displacement field D for hexalayer graphene.

APPENDIX F: TRANSPORT MEASUREMENT OF FOUR DIFFERENT LAYER ABC-STACKED GRAPHENE

Here, we demonstrate several devices with thickness ranging from three to six layers, were fabricated. We also demonstrate the four-terminal resistance as a function of carrier density n and displacement field D measured from the four devices at a temperature of $T = 1.5$ K. The carrier density $n = C_{tg}V_{tg} + C_{bg}V_{bg}$ and displacement field $D = (C_{tg}V_{tg} - C_{bg}V_{bg})/2\varepsilon_0$ can be independently tuned by top gate voltage (V_{tg}) and bottom gate voltage (V_{bg}) applied through the two graphite flaks. Here $C_{tg}(C_{bg})$ is the capacitance between top (bottom) gate and graphene, ε_0 is the vacuum dielectric constant, and e is the elementary charge. The ABC trilayer, tetralayer graphene, and pentalayer graphene were designed to aligned to the top hBN to form moiré superlattices, showing qualitatively similar correlated states at some integer moiré fillings with previous studies (Fig. 7).

[1] M. Koshino, Interlayer screening effect in graphene multilayers with ABA and ABC stacking, Phys. Rev. B **81**, 125304 (2010).

[2] K. F. Mak, J. Shan, and T. F. Heinz, Electronic structure of few-layer graphene: experimental demonstration of strong dependence on stacking sequence, Phys. Rev. Lett. **104**, 176404 (2010).

[3] W. Bao, L. Jing, J. Velasco, Y. Lee, G. Liu, D. Tran, B. Standley, M. Aykol, S. B. Cronin, D. Smirnov, *et al.*, Stacking-dependent band gap and quantum transport in trilayer graphene, Nat. Phys. **7**, 948 (2011).

[4] Y. Lee, D. Tran, K. Myhro, J. Velasco, N. Gillgren, C. N. Lau, Y. Barlas, J. M. Poumirol, D. Smirnov, and F. Guinea, Competition between spontaneous symmetry breaking and single-particle gaps in trilayer graphene, Nat. Commun. **5**, 5656 (2014).

[5] G. Chen, L. Jiang, S. Wu, B. Lyu, H. Li, B. L. Chittari, K. Watanabe, T. Taniguchi, Z. Shi, J. Jung, *et al.*, Evidence of a gate-tunable Mott insulator in a trilayer graphene moiré superlattice, Nat. Phys. **15**, 237 (2019).

[6] C. H. Lui, Z. Li, K. F. Mak, E. Cappelluti, and T. F. Heinz, Observation of an electrically tunable band gap in trilayer graphene, Nat. Phys. **7**, 944 (2011).

[7] M. Aoki and H. Amawashi, Dependence of band structures on stacking and field in layered graphene, Solid State Commun. **142**, 123 (2007).

[8] F. Winterer, F. R. Geisenhof, N. Fernandez, A. M. Seiler, F. Zhang, and R. T. Weitz, Ferroelectric and spontaneous quantum Hall states in intrinsic rhombohedral trilayer graphene, Nat. Phys. **20**, 422 (2024).

[9] K. Liu, J. Zheng, Y. Sha, B. Lyu, F. Li, Y. Park, Y. Ren, K. Watanabe, T. Taniguchi, J. Jia, *et al.*, Spontaneous broken-symmetry insulator and metals in tetralayer rhombohedral graphene, Nat. Nanotechnol. **19**, 188 (2024).

[10] W. Zhou, J. Ding, J. Hua, L. Zhang, K. Watanabe, T. Taniguchi, W. Zhu, and S. Xu, Layer-polarized ferromagnetism in rhombohedral multilayer graphene, Nat. Commun. **15**, 2597 (2024).

[11] T. Han, Z. Lu, G. Scuri, J. Sung, J. Wang, T. Han, K. Watanabe, T. Taniguchi, H. Park, and L. Ju, Correlated insulator and Chern insulators in pentalayer rhombohedral-stacked graphene, Nat. Nanotechnol. **19**, 181 (2023).

[12] H. Zhou, T. Xie, T. Taniguchi, K. Watanabe, and A. F. Young, Superconductivity in rhombohedral trilayer graphene, Nature **598**, 434 (2021).

[13] G. Chen, A. L. Sharpe, P. Gallagher, I. T. Rosen, E. J. Fox, L. Jiang, B. Lyu, H. Li, K. Watanabe, T. Taniguchi, *et al.*, Signatures of tunable superconductivity in a trilayer graphene moire superlattice, Nature **572**, 215 (2019).

[14] H. Zhou, T. Xie, A. Ghazaryan, T. Holder, J. R. Ehrets, E. M. Spanton, T. Taniguchi, K. Watanabe, E. Berg, M. Serbyn, *et al.*, Half- and quarter-metals in rhombohedral trilayer graphene, Nature **598**, 429 (2021).

[15] T. Han, Z. Lu, G. Scuri, J. Sung, J. Wang, T. Han, K. Watanabe, T. Taniguchi, L. Fu, H. Park, *et al.*, Orbital multiferroicity in pentalayer rhombohedral graphene, Nature **623**, 41 (2023).

[16] Y. Sha, J. Zheng, K. Liu, H. Du, K. Watanabe, T. Taniguchi, J. Jia, Z. Shi, R. Zhong, and G. Chen, Observation of a Chern insulator in crystalline ABCA-tetralayer graphene with spin-orbit coupling, Science **384**, 414 (2024).

[17] T. Han, Z. Lu, Y. Yao, J. Yang, J. Seo, C. Yoon, K. Watanabe, T. Taniguchi, L. Fu, F. Zhang, *et al.*, Large quantum anomalous Hall effect in spin-orbit proximitized rhombohedral graphene, Science **384**, 647 (2024).

[18] G. Chen, A. L. Sharpe, E. J. Fox, Y.-H. Zhang, S. Wang, L. Jiang, B. Lyu, H. Li, K. Watanabe, T. Taniguchi, *et al.*, Tunable correlated Chern insulator and ferromagnetism in a moiré superlattice, Nature **579**, 56 (2020).

[19] Z. Lu, T. Han, Y. Yao, A. P. Reddy, J. Yang, J. Seo, K. Watanabe, T. Taniguchi, L. Fu, and L. Ju, Fractional quantum anomalous Hall effect in multilayer graphene, Nature **626**, 759 (2024).

[20] L.-J. Yin, H. Jiang, J.-B. Qiao, and L. He, Direct imaging of topological edge states at a bilayer graphene domain wall, Nat. Commun. **7**, 11760 (2016).

[21] L. Jiang, S. Wang, Z. Shi, C. Jin, M. I. B. Utama, S. Zhao, Y.-R. Shen, H.-J. Gao, G. Zhang, and F. Wang, Manipulation of domain-wall solitons in bi- and trilayer graphene, Nat. Nanotechnol. **13**, 204 (2018).

[22] H. Li, M. I. B. Utama, S. Wang, W. Zhao, S. Zhao, X. Xiao, Y. Jiang, L. Jiang, T. Taniguchi, K. Watanabe, *et al.*, Global control of stacking-order phase transition by doping and electric field in few-layer graphene, Nano Lett. **20**, 3106 (2020).

[23] C. H. Lui, Z. Li, Z. Chen, P. V. Klimov, L. E. Brus, and T. F. Heinz, Imaging stacking order in few-layer graphene, Nano Lett. **11**, 164 (2011).

[24] T. A. Nguyen, J.-U. Lee, D. Yoon, and H. Cheong, Excitation energy dependent Raman signatures of ABA- and ABC-stacked few-layer graphene, Sci. Rep. **4**, 4630 (2014).

[25] C. Cong, T. Yu, K. Sato, J. Shang, R. Saito, G. F. Dresselhaus, and M. S. Dresselhaus, Raman characterization of ABA- and ABC-stacked trilayer graphene, ACS Nano **5**, 8760 (2011).

[26] J. Yu, R. Giridharagopal, Y. Li, K. Xie, J. Li, T. Cao, X. Xu, and D. S. Ginger, Imaging graphene Moire superlattices via scanning kelvin probe microscopy, Nano Lett. **21**, 3280 (2021).

[27] Y. Shan, Y. Li, D. Huang, Q. Tong, W. Yao, W.-T. Liu, and S. Wu, Stacking symmetry governed second harmonic generation in graphene trilayers, Sci. Adv. **4**, eaat0074 (2018).

[28] J. J. Dean and H. M. van Driel, Second harmonic generation from graphene and graphitic films, Appl. Phys. Lett. **95**, 261910 (2009).

[29] T. Ohta, A. Bostwick, J. L. McChesney, T. Seyller, K. Horn, and E. Rotenberg, Interlayer interaction and electronic screening in multilayer graphene investigated with angle-resolved photoemission spectroscopy, Phys. Rev. Lett. **98**, 206802 (2007).

[30] T. Taychatanapat, K. Watanabe, T. Taniguchi, and P. Jarillo-Herrero, Quantum Hall effect and Landau-level crossing of Dirac fermions in trilayer graphene, Nat. Phys. **7**, 621 (2011).

[31] M. F. Craciun, S. Russo, M. Yamamoto, J. B. Oostinga, A. F. Morpurgo, and S. Tarucha, Trilayer graphene is a semimetal with a gate-tunable band overlap, Nat. Nanotechnol. **4**, 383 (2009).

[32] H. Min and A. H. MacDonald, Origin of universal optical conductivity and optical stacking sequence identification in multilayer graphene, Phys. Rev. Lett. **103**, 067402 (2009).

[33] A. McEllistrim, A. Garcia-Ruiz, Z. A. H. Goodwin, and V. I. Fal'ko, Spectroscopic signatures of tetralayer graphene polytypes, Phys. Rev. B **107**, 155147 (2023).

[34] N. M. R. Peres, Colloquium: The transport properties of graphene: An introduction, Rev. Mod. Phys. **82**, 2673 (2010).

[35] L. A. Falkovsky and S. S. Pershoguba, Optical far-infrared properties of a graphene monolayer and multilayer, Phys. Rev. B **76**, 153410 (2007).

[36] K. F. Mak, L. Ju, F. Wang, and T. F. Heinz, Optical spectroscopy of graphene: From the far infrared to the ultraviolet, Solid State Commun. **152**, 1341 (2012).